Accepted Manuscript

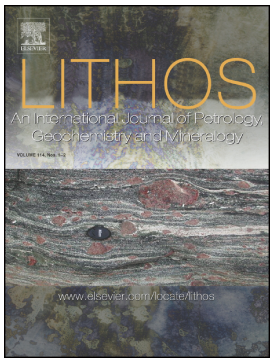


# Geophysical source conditions for basaltic lava from Santorini volcano based on geochemical modeling

Ioannis Baziotis, Jun-Ichi Kimura, Avgoustos Pantazidis, Stephan Klemme, Jasper Berndt, Paul Asimow

PII: S0024-4937(18)30266-4
DOI: doi:10.1016/j.lithos.2018.07.027
Reference: LITHOS 4733

To appear in: *LITHOS*

Received date: 26 April 2018
Accepted date: 26 July 2018

Please cite this article as: Ioannis Baziotis, Jun-Ichi Kimura, Avgoustos Pantazidis, Stephan Klemme, Jasper Berndt, Paul Asimow , Geophysical source conditions for basaltic lava from Santorini volcano based on geochemical modeling. Lithos (2018), doi:10.1016/j.lithos.2018.07.027

Draft for:

Lithos Letters, Research Letter

**Title:**

# Geophysical source conditions for basaltic lava from Santorini volcano based on geochemical modeling

Authors:

Ioannis Baziotis[1], Jun-Ichi Kimura[2], Avgoustos Pantazidis[1], Stephan Klemme[3], Jasper Berndt[3], and Paul Asimow[4]

Affiliations:

[1]Department of Natural Resources Management & Agricultural Engineering, Agricultural University of Athens, Athens, Greece

[2]Department of Solid Earth Geochemistry, Japan Agency for Marine-Earth Science and Technology, Yokosuka 237-0061, Japan

[3]Institut für Mineralogie, Westfälische Wilhelms-Univ. Münster, Correnstrasse 24, Münster, Germany

[4]Division of Geological and Planetary Sciences, California Institute of Technology, Pasadena, California 91125, USA

Correspondence to:

Ioannis Baziotis

ibaziotis@aua.gr

**Abstract** (210 words)

Santorini volcano sits ~145 km above the Aegean Wadati-Benioff zone, where the African plate subducts northward beneath Eurasia. There are only a few localities in the whole Aegean where basaltic lavas primitive enough to constrain mantle processes beneath the Aegean arc can be found; in this work we analyzed one such locality, a basalt lava from the southern part of Santorini. We apply a suite of petrological tools (PRIMACALC2 and ABS5) in sequence to estimate magma chamber conditions, primary magma composition, mantle melting conditions, and slab dehydration conditions. Back-calculation modeling based on major-element chemistry yields shallow magma chamber conditions of $P$ = 0.02 GPa, $fO_2$ = QFM+2, and ~1 wt.% $H_2O$ in the primary magma. The estimated major element composition of this primary magma then leads to estimated mantle melting conditions of 2.1 GPa, 1353°C, and $F$ = 8%; whereas a more precise estimate derived from trace element modeling implies 1.7 GPa, 1323°C, and $F$ = 18%. Furthermore, the trace element model implies a slab flux derived from 4.6 GPa (~150 km slab depth). The estimated slab depth, magma segregation conditions, and magma chamber depth are all consistent with seismic observations, supporting slab dehydration in the seismically imaged steep slab interval and flux melting in a relatively hot mantle wedge.

## 1. Introduction

Santorini volcano, centrally located along the South Aegean arc, sits ~145 km above the Wadati-Benioff zone (WBZ) marking the northward subduction of the African plate beneath the Eurasian continent [*Papazachos et al.*, 2000]. It has a long eruption record: activity started ~650 ka (mainly rhyolites and rhyodacites), with pulses at ~550 ka (basalt-rhyodacite) and ~360 ka (large explosive eruptions of andesite-rhyodacite and minor basalt), culminating in the caldera-forming Bronze-age Minoan event [*Druitt et al.*, 1999]. As in many volcanic arcs, scenarios of fractional crystallization with or without mixing between felsic and mafic magmas have been proposed to explain the broad range of compositions, textures, and eruptive styles of the Santorini volcanic products [*Andújar et al.*, 2015; *Huijsmans et al.*, 1988]. When the goal is specifically to interrogate mantle processes, melting conditions, and source compositions, though, it is always important to identify the least fractionated and contaminated basalt lavas, because information about the early stages of magma genesis are progressively obscured and overprinted during shallow magmatic evolution. Here we focus on a basalt lava flow from the cinder cone of Akrotiri area (344±44 ka; Druitt et al., 1999) located at the southern part of Santorini at Balos cove (36°21.7'N, 25°23.8'E), one of very few basalt exposures along the Aegean arc. The age of this rock is estimated at 344±24 ka

[*Druitt* et al., 1999]. The goals are to constrain both the magma chamber conditions that led to the mafic eruption and the geophysical conditions of the slab and mantle source regions via petrological and geochemical mass balance modeling.

## 2. Basalt Lavas from Santorini Volcano

### 2.1. Analytical methods

We collected 20 lava and scoria samples, selected for freshness and integrity, from the Balos area of southern Santorini. Polished thin sections prepared from selected samples were examined by optical microscopy and scanning electron microscopy for their textures and by electron probe microanalyzer (EPMA) and field emission EPMA (FE-EPMA) for their mineral chemistry. The EPMA analyses were conducted on a JEOL JXA-8900 Superprobe with four wavelength-dispersive spectrometers (WDS) at the Laboratory of Mineralogy and Geology, Agricultural University of Athens, Greece, while additional FE-EPMA data were collected on a JEOL JXA8530F equipped with five WDS and an energy-dispersive spectrometer at the Institut für Mineralogie, University of Münster, Germany. Analyses were conducted at 15 kV accelerating voltage. For minerals, a 20 nA beam current, ~2 μm beam diameter, and counting times of 20 s on peak positions and 10 s for backgrounds were used. For glass analyses, a

defocused beam with ~5 μm diameter, 10 s peak and 5 s background times were used to avoid volatile escape. Natural and synthetic standards used were: quartz (Si), corundum (Al), jadeite (Na), diopside (Ca), olivine (Mg), fayalite (Fe), spessartine (Mn), orthoclase (K), apatite (P), ilmenite (Ti), chromite (Cr), and Ni-oxide (Ni). Matrix effects were corrected by the conventional ZAF method. Representative mineral chemistry results are given in **Table 1**.

Whole-rock major and trace element concentrations were determined on pellets of pressed rock powder using the X-ray fluorescence spectrometer (Panalytical PW-2400) at the Hellenic Centre for Marine Research, Greece. X-ray counts were converted to concentrations using the Panalytical Axios ProTrace standards and protocol, which includes 500 ppm and 1000 ppm concentration standards for each of 40 elements, calibrated against more than 200 international reference materials. The analytical precision is 5-10% on the basis of duplicate runs of standards and unknowns, except for those trace elements whose concentrations are close to their detection limits, for which analytical precision may be ~50% [*Barreda et al.,* 2016]. Accuracy is assessed using the secondary geological standard PACS-2, for those elements included in the protocol and also assigned a standard reference value in PACS-2. Reported detection limits are based on count rates and background statistics. Whole-rock chemistry results, reference and

measured values of the PACS-2 standard, and detection limits are given in **Table 2**.

### 2.2. Petrography and mineral chemistry

The basalt lavas from Santorini contain phenocrysts of olivine and clinopyroxene in a groundmass of olivine, clinopyroxene, plagioclase, and magnetite with minor glass and rare xenocrystic quartz. The basalts exhibit pilotaxitic to trachytic textures defined by random to flow-oriented tabular plagioclases, respectively. Their modes include 10–12 vol.% olivine, 10–15 vol.% clinopyroxene, and 45–50 vol.% plagioclase. The olivine phenocrysts are 0.5–1.0 mm in length, pale pink in color, euhedral to subhedral in shape, and commonly cracked. The large olivine crystals are complexly zoned in forsterite content. Reversely zoned cores increasing outwards from $Fo_{79–81}$ to maxima of $Fo_{84.5}$ are surrounded by normally zoned mantles trending down to well-defined uniform rims 3-20 μm wide of $Fo_{71.9}$ in direct contact with groundmass (**Fig. 1a**, **Table 1**). Small olivine microphenocrysts <0.1 mm in diameter occur within the groundmass and show minor normal zonation ($Fo_{75-71}$) (**Figs. 1a, b**).

Clinopyroxene, pale green in polarized light, is present as phenocrysts up to 600 μm long and groundmass crystals <100 μm long (**Fig. 1c**). Both sizes have compositions in the range $En_{36–48}Wo_{41–44}Fs_{11–21}$.

Embedded in a flow texture, 100–200 μm prismatic or dendritic plagioclase grains form the most abundant mineral phase in the groundmass (**Figs. 1c, d**). Plagioclase crystals display normal zoning, richer in calcium in the cores ($An_{78–85}$) than in the rims ($An_{60–76}$).

The less mafic samples contain a minor fraction (~1–2 vol.%) of idiomorphic to subidiomorphic magnetite <20 μm in diameter, with variable $TiO_2$ (1.9-16.5 wt.%) (**Fig. 1e**). Scarce subhedral to anhedral xenocrystic quartz grains are present in the groundmass (**Fig. 1f**).

### 2.3. Bulk rock chemistry

The major element composition of the basalt lavas occupies a narrow range, with 49.0–51.2 wt.% $SiO_2$, 10.6–11.1 wt.% CaO, 8.3–9.3 wt.% FeO, 5.9–6.4 wt.% MgO, and 2.0–2.2 wt.% $Na_2O$ (**Table 2**). On the basis of total alkalis ($Na_2O$ + $K_2O$) versus silica, most of the samples lie in the basalt field (Le Bas et al. 1986; figure not given), though one sample plots very close to the basaltic andesite field. Other oxides ($P_2O_5$, MnO, $TiO_2$, and $K_2O$) are <1 wt.%. To plot trace element patterns, since we have only XRF data on our new samples, we used abundances of unanalyzed elements such as Sm, Eu, heavy rare earth elements (HREE; Tb, Yb, Lu), and U from previously reported analytical results on similar Santorini basalts [*Michaud et al.*, 2000], and interpolated

the remaining HREE by assuming smooth patterns in normalized multi-element plots (see **Table 3**). Trace elements exhibit typical arc-basalt signatures, with negative Nb anomaly, positive Sr and Pb spikes, enrichments of large ion lithophile elements, and flat patterns of the mid- to heavy rare earth elements in normalized multi-element plots (**Fig. 2a**, **Table 3**).

## 3. Geochemical Modeling

Geophysical parameters such as the segregation depth of magma from the mantle and fractionation depth in a crustal magma chamber can be estimated using phase equilibria [*Almeev et al.*, 2013; *Herzberg and Asimow*, 2015; *Kuritani et al.*, 2014; *Till et al.*, 2012] or mineral-melt partitioning [*Putirka*, 2005]. We apply two petrological/geochemical mass balance models based on major and trace elements, respectively.

The PRIMACALC2 model [*Kimura and Ariskin*, 2014] uses major element chemistry of a fractionated magma and a thermodynamic model of mineral-melt equilibrium to estimate the pressure ($P$), temperature ($T$), oxygen fugacity ($fO_2$), and water content ($X_{H_2O}$) prevailing during fractional crystallization in the shallow magma chamber. The PRIMACALC2 code also estimates both major and trace element

composition of the primary magma by incrementally adding calculated equilibrium mineral phases back into the magma composition. The major element composition of the primary magma, in turn, is used to estimate the *P*, *T*, and degree of partial melting (*F*) at which the magma might have been in equilibrium with a mantle peridotite residue, based on experimentally-determined and mass-balance constrained petrogenetic grids for mantle melting.

The second model is Arc Basalt Simulator version 5 (ABS5) [*Kimura*, 2017]. Taking the incompatible trace element compositions of the primary basalt magma from PRIMACALC2 as input, ABS5 forward-calculates slab dehydration/melting, assuming compositions of slab mantle, gabbro, basalt, and sediment and a set of partition coefficients. Incompatible element compositions of slab-derived liquids are estimated for slab depths equivalent to 0.5–6 GPa and subsequently input to mass-balance-constrained open-system flux melting calculations of primary basalt compositions for a range of mantle source depletion at conditions in the range of 0.8–3 GPa and 1000–1450 °C. A Monte Carlo sampling of the resulting model primary basalts is compared to the major and trace element compositions of the primary magma estimated by PRIMACALC2 to locate the best fit and thereby estimate the *P*-*T* conditions of slab fluid extraction ($P_{slb}$ and $T_{slb}$) and conditions of flux melting of the

mantle — *P*, *T*, *F*, fraction of slab fluid ($f_{slb\ liq}$), and degree of depletion of the mantle *(%MORBext*) relative to primitive mantle (PM) or depleted mid-ocean ridge basalt source mantle (DMM).

The assumptions, modeling strategy, and calculation details for both PRIMACALC2 [*Kimura and Ariskin*, 2014] and ABS5 [*Kimura*, 2017] are given in the literature. Both models are coded in macro-enabled Microsoft Excel© spreadsheets and can be downloaded along with the online versions of the above references.

### 3.1. Primary Magma

The basaltic samples analyzed here are by far the most primitive samples available from Santorini and are therefore the best samples for application of a primary melt calculation. None of the evolved samples from Santorini help to constrain the primary basalt composition, and in fact within error each of them can be derived by continued fractionation of the primitive basalts reported here. Also, because our sample population is nearly homogeneous, we chose the average of all whole-rock analyses as a target for the PRIMACALC2 model. Some trace elements required by the model are missing and were supplemented either from the literature [*Michaud et al.*, 2000] or from assumptions in the multi-element plot (**Fig. 2a**, **Table 3**). Calculated magma chamber

conditions of the representative Santorini basalt and the source mantle conditions of its primary basalt are summarized in **Table 3**, together with the fitted major and trace element compositions of the evolved basalt, the primary basalt estimate from PRIMACALC2 and best-fitting primary basalt from ABS5. The full results of the fractional crystallization sequence from the primary liquid to the erupted Santorini basalt are given in **Table S1,** based on the thermodynamic model COMAGMAT 3.7.2 [*Ariskin*, 1999], a module in PRIMACALC2.

The fractionation calculation gave best results for magma chamber conditions of $P$ = 0.02 GPa, $fO_2$ = QFM+2 (estimated from mineral chemistry), and $X_{H_2O}$ = 1.0 wt.%. The estimated total degree of crystallization is ~70% and the path includes (in sequence) olivine, plagioclase, magnetite and clinopyroxene fractionation (**Fig. 2b**). Calculated masses of each fractionated phase are 17 vol.% olivine, 20-25 vol.% clinopyroxene, 22-25 vol.% plagioclase, and ~5 vol.% magnetite. Although there is no particular reason these proportions of fractionated phases should correspond to the observed mode of the erupted basalt, the proportions are consistent with the observed mode of 10–12 vol.% olivine, 10–15 vol.% clinopyroxene, 45–50 vol.% plagioclase, and ~5 vol.% magnetite. Calculated mineral compositions are $Fo_{84}$ for olivine, $En_{52}Wo_{40}Fs_9$ for clinopyroxene, and $An_{70–80}$ for plagioclase in the final fractionation

stage, all of which are consistent with the observed core compositions of the corresponding phenocrysts, $Fo_{81}$, $En_{48}Wo_{41}Fs_{11}$, and $An_{78–85}$ (**Fig. 2b**, **Table S1**).

This model provides a reasonable estimate for a primary magma with Mg# = 0.76 (Mg#=Mg/[Mg+$Fe^{2+}$]) containing $Fo_{91}$ olivine that would be in equilibrium with a residual mantle peridotite having MgO = 43 wt.% (**Table 3**). The estimated Ni content in the olivine is 0.34 wt.%, slightly lower than required for equilibrium with the mantle, but the difference is within the uncertainties in olivine-melt Ni partition coefficients. Estimated melting conditions of the mantle source based only on the best-fit to the major-element composition of the primary magma estimate are $P$ = 2.1 GPa, $T$ = 1353 °C, and $F$ = 7.6%, with $X_{H_2O}$ = 1 wt.% in the primary basalt (**Fig. 2c**, **Table 3**).

Crustal assimilation might also have affected the elemental abundances in the estimated primary magma. There are reports of increases or decreases due to assimilation of up 10 % in the elemental abundances of basalt to basaltic andesite rocks in an arc with ~30 km thick crust (e.g., NE Japan) [*Kimura and Yoshida*, 2006]. However, ±20% differences in the elemental abundances in the model primary basalt magma cause <10% changes in estimated slab and mantle conditions, except for the degree of source mantle depletion, which may be affected by a factor of two as shown by the sensitivity tests of ABS5 [*Kimura*, 2017]. The same has been shown for

PRIMACALC2 [*Kimura and Ariskin*, 2014]. We therefore consider that the effects of crustal assimilation in this case are likely negligible for most of the reported conclusions.

### 3.2. Source Mantle and Slab Conditions

Using the estimated primary basalt composition from PRIMACALC2, we calculated source conditions using ABS5. We used the global sediment composite (GLOSS) composition [*Plank and Langmuir*, 1988] as an estimate of the sedimentary component of the slab because the average compositions of Aegean sediments have a similar compositional range, although large variations are seen in Ba, U, Sr and Zr–Hf concentrations [*Klaver et al.*, 2015]. For the subducted oceanic crust composition, we considerd both typical altered oceanic crust (AOC) [*Kelley et al.*, 2003] and normal mid-ocean ridge basalt (N-MORB) [*Jenner and O'Neill*, 2012]. The mantle wedge source was initially assumed to have PM composition [*Sun and McDonough*, 1989], but prior depletion of this source was examined by fitting the model parameter *%MORBext*, which parameterizes the degree of fractional extraction of MORB melt from PM prior to its advection into the mantle wedge [*Kimura et al.*, 2010] (**Table S2**).

Isotopic compositions of sources and primitive basalt can be used as additional mass balance constraints in ABS5 [*Kimura*, 2017; *Kimura et al.*, 2010; *Kimura et al.*,

2014; *Kimura and Nakajima*, 2014], but in the absence of comprehensive data for the local subducting components we restricted our analysis to major and trace elemental concentrations only. Nevertheless, the resulting estimates of source conditions are reasonably well-constrained (**Table 3**), similar to results from other applications of ABS3 without isotopic constraints [*Rooney and Deering*, 2014]. The ABS5 results are dominantly constrained by mass balance of incompatible trace elements, with additional constraints from major elements [*Kimura*, 2017]. We note that only a one-dimensional family of slab *P-T* conditions is considered, with the relationship between them fixed by subduction parameters such as slab age, slab angle, and subduction rate. These were estimated from a geodynamic model for the Aegean arc [*Syracuse et al.*, 2010; *van Keken et al.*, 2011].

The resultant fits for the incompatible elements are graphically shown in **Figure 2a,** along with the estimated mantle and slab liquid compositions. **Table 3** shows the results for major and trace elements and the slab-mantle conditions. The forward calculations reproduce well the incompatible element abundances in the primary basalt, except for Ba, Th, and U, which are affected by minor minerals in the slab and by the detailed proportions of different sedimentary components in the subducted section [*Kimura et al.*, 2014]. It is notable that the important geophysical parameter estimates

for melting conditions are similar to those from PRIMACALC2 apart from a large difference in $F$: $P$ = 1.7 (2.1) GPa, $T$ = 1323 (1353) °C, $F$ = 18.5 (7.6) %, and primary basalt $X_{H_2O}$ = 1.55 (1.01) wt.% (values in parentheses from PRIMACALC2). The best-fitting slab fluid composition is that derived from $P_{slab}$ = 4.4 GPa at $T_{slab}$ = 799°C, conditions where both sediment- and basalt-derived fluids are supercritical [*Kawamoto et al., 2012*]. Slab flux added to the mantle is found to make up ~5.4 wt.% of the source. The best-fitting source mantle is depleted relative to PM by *%MORBext* = 5.5 wt.%. This depleted source is similar to or only slightly more fertile than DMM [*Asimow et al.*, 2004; *Kimura and Kawabata*, 2015](**Fig. 2a**). Furthermore, the best-fitting slab fluid is dominated by the altered oceanic crust component: it is a mix of 10% sediment-derived and 90% AOC-derived fluxes (see *Fliq*[*SED*] and *Fliq*[*AOC*] in **Table 3**). Recently, isotopic compositions from Aegean sediments have become available and the contribution of slab sediments to the Aegean arc lavas has been discussed [*Klaver et al.*, 2016; *Klaver et al.*, 2015]. The results suggested a range of at least 2% to at most 10% sediment-derived component in the Santorini arc lava source.

## 4. Seismic Observations and Geochemical Models

Combining petrological and geochemical estimates of slab and mantle conditions with

geophysical observations can lead to a more unified understanding of the structure of a subduction system [*Kimura*, 2017; *Kimura et al.*, 2010; *Kimura et al.*, 2014; *Kimura and Nakajima*, 2014; *Kimura et al.*, 2009]. The excellent agreement between the estimated source mantle conditions from the backward PRIMACALC2 and the forward ABS5 models offers a useful basis for comparison to geophysical inferences from local seismological observations. **Figure 3a** shows a seismicity map of the Aegean, including seismic foci in the subducting African plate, in the mantle wedge, and in the upper Eurasian plate [*Papazachos et al.*, 2000]. Recent papers have focused on receiver function analysis to locate the slab surface, as opposed to the classical use of seismicity depths that define the WBZ. Receiver function estimates yield depths to the slab surface beneath Santorini ranging between 100 and 170 km [*Endrun et al.*, 2005; *Olive et al.*, 2014; *Sodoudi et al.*, 2006]. Tomography and receiver function evidence suggest that the subduction angle of the African slab steepens at 100 km and flattens again at 170 km depths. Santorini volcano sits between the 100 km and 170 km contours, within the narrow map-view band above the steep part of the slab, with a best estimate slab depth below the volcano of ~130 km, whereas the WBZ defined by seismicity lies at ~145 km depth under Santorini.

The two estimates of slab depth beneath Santorini, 130 km by receiver function

analysis and 145 km from seismicity, both correlate well with our estimate of slab fluid release at $P$ = 4.4 GPa (~145 km deep), considering the large uncertainty in the estimate of the depth of slab fluid release from the ABS5 petrological model. Furthermore, the upwelling trajectory of the slab fluid can easily be deflected from vertical either by suction towards the wedge corner or by entrainment in the horizontal component of the mantle wedge flow, as suggested by geodynamic models [*Wada and Behn*, 2015] (see **Fig. 3b**). The depth calculated for last equilibration of the primary magma with the fluxed mantle wedge, $P$ = 1.7 GPa (~56 km), is located in the middle of the mantle wedge at a depth where no seismic foci have been observed (**Fig. 3b**).

Using seismicity data, however, we can make the interesting observation that the calculated depth of magma segregation correlates well with the downdip limit of shallow slab-surface seismicity at ~70 km. This may represent the lithosphere-asthenosphere boundary beneath the upper plate of the subduction system, which is the most logical location for melt segregation to occur and where a change in mechanical coupling to the slab may occur (**Fig. 3b**). A similar observation of decreasing slap-top seismicity in the 60–80 km depth range beneath NE Japan has been attributed to a loss of slab-mantle coupling [*Shiina et al.*, 2013].

More generally, the seismic structure beneath the Aegean arc is fundamentally

similar to that observed in the NE Japan arc [*Kimura and Nakajima*, 2014; *Nakajima et al.*, 2013; *Shiina et al.*, 2013]. Yet, the Aegean arc is missing the low-K tholeiitic basalts commonly found in the volcanic front chains of the NE Japan arc. The high *T-P* (1323 °C and 1.7 GPa) calculated here for the center of the Aegean arc are instead similar to those beneath the rear-arc volcanic chain in NE Japan. Although the slab subduction angles of the two arcs are almost identical, the subducted plate in the Aegean Arc is older (200 Ma) than that in the NE Japan arc (129 Ma) [*Syracuse et al.*, 2010], the subduction velocity is much slower in the Aegean than in NE Japan (1.5 cm/yr versus 8.2 cm/yr), and the arc-trench distance is shorter in the Aegean (250 km) than in NE Japan (319 km) [*Syracuse et al.*, 2010]. These observations could be reconciled if the slow subduction rate leads to higher slab temperature at given depth (despite the old slab age) and a reduced arc-trench distance in the Aegean arc. The restricted space available to the mantle wedge at the volcanic front may reduce penetration of hot mantle counterflow into the forearc. This may result in a cold forearc mantle nose, preventing generation of hydrous low-K basalt magma above the shallow (~100 km) slab despite aqueous slab fluids being selectively released at this depth. It is possible that the fluids released into the cold mantle nose from the slab form hydrated mantle that is then advected downwards by slab-mantle coupling [*Wada and Behn*, 2015] and subsequently

dehydrated again at 4.4 GPa depth; in this case the estimate of dehydration depth from ABS5 would correspond to this secondary dehydration event rather than the original slab dehydration.

The agreement between the depth of slab fluid separation beneath Santorini estimated from the geochemical mass balance model and its coincidence with the depth to the WBZ based on seismicity observations is encouraging and supports a more robust description of slab and mantle conditions beneath Santorini. For example, it implies that the path of fluid and melt ascent from the slab surface to Santorini does not depart very much from vertical, which supplies an important constraint on the parameters of geodynamic flow models for the Aegean subduction system. Furthermore, the result lends credence to the notion that the narrowness of the volcanically active front in the Aegean is tied to focused slab dewatering within the interval of steep slab dip.

The results of this study also have implications for two broader issues in subduction zones worldwide: the occurrence of low-K tholeiite and the temperature of mantle wedges. The absence of low-K tholeiite is typical of hot subduction zones such as Cascadia and SW Japan. The same is true for intermediate-temperature subduction systems such as S. Chile. Even in a cold subduction system such as the Marianas, a steep slab angle may prevent production of low-K tholeiite [*Kimura*, 2017]. Scarce

low-K tholeiites do appear in old and cold subduction systems with relatively low subduction angles (<40°), such as NE Japan, northern Izu, and northern Tonga arcs [*Syracuse et al.*, 2010]. The Aegean arc is characterized by a relatively old slab, slow subduction rate, and locally steep slab dip beneath the volcanic front but a generally low slab dip and, we argue here, an anomalously hot mantle wedge despite the old slab age. Hence the absence of low-K tholeiite at Santorini adds a new perspective to theories about which subduction parameters are the prime controls on cross-arc geochemical variations; evidently subduction geometry, slab age, and temperature of mantle wedge inflow are all significant.

The maximum wedge mantle temperatures estimated by geodynamic models of subduction zones worldwide are surprisingly variable [*Syracuse et al.*, 2010]. For cold-slab subduction zones, temperature estimates include 1377 °C (Izu), 1413 °C (NE Japan), and 1451 °C (Tonga). Subduction zones with intermediate-temperature slabs show similar temperatures, such as 1428 °C in S. Chile. Surprisingly, hot-slab subduction zones yield lower estimates of peak mantle-wedge temperature, e.g., 1291 °C in Cascadia. The geodynamically estimated maximum wedge mantle temperature for Aegean arc is quite low, 1275 °C [*Syracuse et al.*, 2010], somewhat similar to estimates for hot-slab subduction systems that lack low-K tholeiite. The

application of ABS5 model calculations to worldwide subduction systems, in contrast, yields relatively coherent results for mantle wedge temperature that are not anti-correlated with slab age. For example, wedge mantle temperature ranges from ABS5 include 1230–1260 °C (NE Japan), 1200–1330 °C (N-Izu), 1250–1370 °C (SW Japan) [*Kimura*, 2017; *Kimura et al.*, 2010], and 1323 °C for the Aegean arc [this study). The ABS5 model uses a geochemical mass balance including water, whose influence buffers the mantle wedge temperature and lowers the solidus temperature of both mantle peridotite and slab components. By contrast, the geodynamic model methd of *Syracuse et al.* [*Syracuse et al.*, 2010] does not explicitly account for the effects of water. The ~50 °C discrepancy in estimates of mantle wedge temperature for the Aegean arc from geodynamics and geochemistry calls for further examination by future work that tests in detail the predictions of each class of model against all available kinds of observations.



**Acknowledgments**

J.I.-K. was funded by JSPS KAKENHI grant #JP15H02148, #JP16H01123, and #JP18H04372. PDA's participation in this study was funded by the US NSF, award EAR-1550934.

**References**

Almeev, R. R., A. A. Ariskin, J.-I. Kimura, and G. S. Barmina (2013), The role of polybaric crystallization in genesis of andesitic magmas: Phase equilibria simulations of the Bezymianny volcanic subseries, *Journal of Volcanology and Geothermal Research*, *263*, 182-192, doi:10.1016/j.jvolgeores.2013.01.004.

Andújar, J., B. Scaillet, M. Pichavant, and T. H. Druitt (2015), Differentiation conditions of a basaltic magma from Santorini, and its bearing on the production of andesite in arc settings, *Journal of Petrology*, *56*(4), 765-794, doi:10.1093/petrology/egv016.

Ariskin, A. A. (1999), Phase equilibria modeling in igneous petrology: use of COMAGMAT model for simulating fractionation of ferro-basaltic magmas and the genesis of high-alumina basalt, *Journal of Volcanology and Geothermal Research*, *90*(1), 115-162, doi:10.1016/S0377-0273(99)00022-0.

Asimow, P. D., J. E. Dixon, and C. H. Langmuir (2004), A hydrous melting and fractionation model for mid-ocean ridge basalts: Application to the Mid-Atlantic Ridge near the Azores, *Geochemistry, Geophysics, Geosystems*, *5*(1), doi:10.1029/2003GC000568.

Barreda, M. F. G., Edo, M. R., Cordero, M. O., and Vaquer, M. J. V. (2016), Determination of minor and trace elements in geological materials used as raw ceramic materials, *boletín de la sociedad española de cerámica y vidri*o, 55(5), 185-196.

Druitt, T. H., L. Edwards, R. M. Mellors, D. M. Pyle, R. S. J. Sparks, M. Lanphere, M. Davies, and B. Barriero (1999), Santorini Volcano, in *Geological Society of London, Memoirs*, edited, p. 165.

Endrun, B., L. Ceranna, T. Meier, M. Bohnhoff, and H. P. Harjes (2005), Modeling the influence of Moho topography on receiver functions: A case study from the central Hellenic subduction zone, *Geophysical Research Letters*, *32*(12), doi:doi:10.1029/2005GL023066.

Herzberg, C., and P. D. Asimow (2015), PRIMELT3 MEGA.XLSM software for primary magma calculation: Peridotite primary magma MgO contents from the liquidus to the solidus, *Geochemistry, Geophysics, Geosystems*, *16*(2), 563-578, doi:10.1002/2014GC005631.

Huijsmans, J. P. P., M. Barton, and V. J. M. Salters (1988), Geochemistry and evolution of the calc-alkaline volcanic complex of Santorini, Aegean Sea, Greece, *Journal of*

*Volcanology and Geothermal Research*, *34*, 283-306.

Jenner, F. E., and H. S. C. O'Neill (2012), Analysis of 60 elements in 616 ocean floor basaltic glasses, *Geochemistry, Geophysics, Geosystems*, *13*(2), doi:10.1029/2011GC004009.

Kelley, K. A., T. Plank, J. Ludden, and H. Staudigel (2003), Composition of altered oceanic crust at ODP Sites 801 and 1149, *Geochemistry Geophysics Geosystems*, *4*, doi:10.1029/2002GC000435.

Kimura, J.-I. (2017), Modeling chemical geodynamics of subduction zones using the Arc Basalt Simulator version 5, *Geosphere*, *13*(4), 992-1025, doi:10.1130/GES01468.1.

Kimura, J.-I., J. R. K. Adam, M. Rowe, N. Nakano, M. Katakuse, P. van Keken, B. Hacker, and R. J. Stern (2010), Origin of cross-chain geochemical variation in Quaternary lavas from northern Izu arc: A quantitative mass balance approach on source identification and mantle wedge processes, *Geochemistry Geophysics Geosystems*, doi:10.1029/2010GC003050.

Kimura, J.-I., and A. A. Ariskin (2014), Calculation of water-bearing primary basalt and estimation of source mantle conditions beneath arcs: PRIMACALC2 model for WINDOWS, *Geochemistry Geophysics Geosystems*, *15*, doi:10.1002/2014GC005329.

Kimura, J.-I., et al. (2014), Diverse magmatic effects of subducting a hot slab in SW Japan: results from forward modeling, *Geochemistry Geophysics Geosystems*, *15*, doi: 10.1002/2013GC005132.

Kimura, J.-I., and H. Kawabata (2015), Ocean Basalt Simulator version 1 (OBS1): Trace element mass balance in adiabatic melting of a pyroxenite-bearing peridotite, *Geochemistry, Geophysics, Geosystems*, *16*(1), 267-300, doi:10.1002/2014GC005606.

Kimura, J.-I., and J. Nakajima (2014), Behaviour of subducted water and its role in magma genesis in the NE Japan arc: A combined geophysical and geochemical approach, *Geochimica et Cosmochimica Acta*, *143*, 165-188, doi:10.1016/j.gca.2014.04.019.

Kimura, J.-I., P. van Keken, B. R. Hacker, H. Kawabata, T. Yoshida, and R. J. Stern (2009), Arc Basalt Simulator (ABS) version 2, a simulation model for slab dehydration, fluid-mantle reaction, and fluid-fluxed mantle melting for arc basalts: modeling scheme and application, *Geochemistry Geophysics Geosystems*, *7*, doi:10.1029/2008GC002217.

Kimura, J.-I., and T. Yoshida (2006), Contributions of slab fluid, mantle wedge and crust to the origin of Quaternary lavas in the NE Japan arc, *Journal of Petrology*, *47*, 2185–2232.

Klaver, M., S. Carey, P. Nomikou, I. Smet, A. Godelitsas, and P. Vroon (2016), A distinct source and differentiation history for Kolumbo submarine volcano, Santorini

volcanic field, Aegean arc, *Geochemistry, Geophysics, Geosystems*, *17*(8), 3254-3273, doi:doi:10.1002/2016GC006398.

Klaver, M., T. Djuly, S. de Graaf, A. Sakes, J. Wijbrans, G. Davies, and P. Vroon (2015), Temporal and spatial variations in provenance of Eastern Mediterranean Sea sediments: Implications for Aegean and Aeolian arc volcanism, *Geochimica et Cosmochimica Acta*, *153*, 149-168, doi:10.1016/j.gca.2015.01.007.

Kuritani, T., T. Yoshida, J.-I. Kimura, T. Takahashi, Y. Hirahara, T. Miyazaki, R. Senda, Q. Chang, and Y. Ito (2014), Primary melt from Sannome-gata volcano, NE Japan arc: constraints on generation conditions of rear-arc magmas, *Contributions to Mineralogy and Petrology*, *167*(2), 969, doi:10.1007/s00410-014-0969-7.

Michaud, V., R. Clocchiatti, and S. Sbrana (2000), The Minoan and post-Minoan eruptions, Santorini (Greece), in the light of melt inclusions: chlorine and sulphur behaviour, *Journal of Volcanology and Geothermal Research*, *99*(1), 195-214, doi:10.1016/S0377-0273(00)00173-6.

Nakajima, J., S. Hada, E. Hayami, N. Uchida, A. Hasegawa, S. Yoshioka, T. Matsuzawa, and N. Umino (2013), Seismic attenuation beneath northeastern Japan: Constraints on mantle dynamics and arc magmatism, *Journal of Geophysical Research: Solid Earth*, *118*(11), 5838-5855, doi:10.1002/2013JB010388.

Olive, J.-A., F. Pearce, S. Rondenay, and M. D. Behn (2014), Pronounced zonation of seismic anisotropy in the Western Hellenic subduction zone and its geodynamic significance, *Earth and Planetary Science Letters*, *391*, 100-109, doi:10.1016/j.epsl.2014.01.029.

Papazachos, B. C., V. G. Karakostas, C. B. Papazachos, and E. M. Scordilis (2000), The geometry of the Wadati-Benioff zone and lithospheric kinematics in the Hellenic arc, *Techtonophysics*, *319*, 275-300.

Plank, T., and C. H. Langmuir (1988), An evaluation of the global variations in the major element chemistry of arc basalts, *Earth and Planetary Science Letters*, *90*, 349-370.

Putirka, K. D. (2005), Mantle potential temperatures at Hawaii, Iceland, and the mid-ocean ridge system, as inferred from olivine phenocrysts: Evidence for thermally driven mantle plumes, *Geochemistry, Geophysics, Geosystems*, *6*(5), doi:10.1029/2005GC000915.

Rooney, T. O., and C. D. Deering (2014), Conditions of melt generation beneath the Taupo Volcanic Zone: The influence of heterogeneous mantle inputs on large-volume silicic systems, *Geology*, *42*(1), 3-6, doi:10.1130/g34868.1.

Shiina, T., J. Nakajima, and T. Matsuzawa (2013), Seismic evidence for high pore

pressures in the oceanic crust: Implications for fluid-related embrittlement, *Geophysical Research Letters*, *40*(10), 2006-2010, doi:10.1002/grl.50468.

Sodoudi, F., R. Kind, D. Hatzfeld, K. Priestley, W. Hanka, K. Wylegalla, G. Stavrakakis, A. Vafidis, H. P. Harjes, and M. Bohnhoff (2006), Lithospheric structure of the Aegean obtained from P and S receiver functions, *Journal of Geophysical Research: Solid Earth*, *111*(B12), doi:doi:10.1029/2005JB003932.

Sun, S.-s., and W. F. McDonough (1989), Chemical and isotopic systematics of oceanic basalts: implications for mantle composition and processes., in *Magmatism in the Ocean Basins*, edited by A. D. Saunders and M. J. Norry, pp. 313-345, Geological Society Special Publication, London.

Syracuse, E. M., P. E. van Keken, and G. A. Abers (2010), The global range of subduction zone thermal models, *Physics of the Earth and Planetary Interiors*, doi:10.1016/j.pepi.2010.1002.1004.

Till, C. B., T. L. Grove, and M. J. Krawczynski (2012), A melting model for variably depleted and enriched lherzolite in the plagioclase and spinel stability fields, *Journal of Geophysical Research*, *117*, 10.1029/2011jb009044, doi:B06206 10.1029/2011jb009044.

van Keken, P. E., B. R. Hacker, E. M. Syracuse, and G. A. Abers (2011), Subduction factory: 4. Depth-dependent flux of $H_2O$ from subduction slabs worldwide, *Journal of Geophysical Research*, *116*, 1-15, doi:10.1029/2010JB007922,.

Wada, I., and M. D. Behn (2015), Focusing of upward fluid migration beneath volcanic arcs: Effect of mineral grain size variation in the mantle wedge, *Geochemistry, Geophysics, Geosystems*, *16*(11), 3905-3923, doi:10.1002/2015GC005950.

**Figure Captions**

**Figure 1.** Backscattered electron images of the phenocrysts in the Santorini basalt: (a,b) olivine, (c) clinopyroxene, (d) groundmass with plagioclase, (e) magnetite, and (f) a quartz xenocryst.

**Figure 2.** Calculation results of (a) ABS5 and (b, c) PRIMACALC2 models. (a) Fitting result of ABS5 model melt composition to the Santorini primary basalt trace element composition. Estimated slab fluid and mantle peridotite compositions are also shown (*see* **Table 3**). (b) Estimated crystallization sequence of the Santorini basalt in an oxidized ($fO_2$ = QFM+2) shallow (P = 0.02 GPa) magma chamber with $X_{H_2O}$ = 1 wt.% water in the primary magma. Fractionated mineral phases, percent crystallization, Fo% of olivine, An% of plagioclase, and $X_{H_2O}$ in the magma are all shown as functions of temperature. Vertical lines mark the points along the liquid line of descent of the primary basalt and the observed average Santorini basalt. The horizontal arrow indicates the extent of back-crystallization that leads to the primary magma estimate from PRIMACALC2. (c) CMAS normative mineral projection from the DI apex onto the OL–AN–QZ plane, showing contours of pressure (*P*, solid lines) and extent of melting

(*F*, dotted lines) for batch melting of peridotite. The small circles and arrow show the back calculation trajectory for fractional crystallization of the Santorini basalt and the large black dot indicates the PRIMACALC2 primary basalt solution for Santorini.

**Figure 3.** Seismic structure and estimated geophysical conditions for the Aegean subduction zone and basalt source of the Santorini volcano. (a) Map-view distribution of seismic foci and location of the Santorini volcano. Earthquake symbols indicate magnitude and depth. The location of the cross section are shown. (b) Cross section beneath of the Aegean Arc; seismic foci are perpendicularly projected onto the cross section (open circles). Intra-crustal (shallow) and slab-mantle (deep) seismicity are clearly separated. Small arrows indicate direction of maximum tensile stress from the focal mechanisms. Grey-scaled lines indicate different slab layers used for modeling in ABS5 (from top to bottom: metasomatized mantle wedge peridotite, sediment, altered uppermost oceanic crust, lower (fresh) extrusive basalt, dike, upper gabbro, lower gabbro, and slab peridotite layers). Small filled circles on the slab layers areas of melt or fluid production according to the ABS5 slab model [*Kimura*, 2017], using a *P-T* path for the slab appropriate to the geodynamics of the Aegean arc [*Syracuse et al.*, 2010; *van Keken et al.*, 2011]. Large grey circles and ovals indicate the location and conditions of

the regions of slab fluid derivation, primary magma segregation, and shallow magma chamber (Labeled by pressure, temperature, and key mass-balance variables given and defined in Table 3). Seismicity is sparse in the molten slab region and mantle wedge, whereas the shallow magma chamber is located in the brittle upper crust. The change in seismicity and stress field in the slab at ~70 km may be associated with penetration into the convecting mantle wedge asthenosphere. The thermal structure estimated by ABS5 modeling is consistent with this tectonic setting (see the 800 and 1300 °C isotherms).

**Table Captions**

**Table 1.** Major element mineral chemistry of the Santorini samples.

**Table 2.** Whole-rock major and trace element compositions of the Santorini basalt lavas.

**Table 3.** Calculated results of primary basalt magma by PRIMACALC2 and its source conditions estimated by ABS5 models. Input column indicates average composition of the Santorini basalt. Data are from this study (bold), from [*Michaud et al.*, 2000] (regular), and estimated from other elements (italic).

**Table 1: Major element mineral chemistry of the Santorini samples.**

| | Ol-1 | Ol-2 | Ol-3 | Ol-4 | Pl-1c | Pl-1r | Pl-2c | Pl-2r | Cpx-1 | Cpx-2 | Cpx-3 |
|---|---|---|---|---|---|---|---|---|---|---|---|
| $SiO_2$ | 38.8 | 39.3 | 40.4 | 41.4 | 51.7 | 53.3 | 50.3 | 50 | 50.2 | 52.7 | 45.3 |
| $TiO_2$ | <b.dl | <b.dl | <b.dl | <b.dl | <b.dl | <b.dl | <b.dl | <b.dl | <b.dl | <b.dl | <b.dl |
| $Al_2O_3$ | <b.dl | <b.dl | <b.dl | <b.dl | 30.5 | 29.5 | 31.1 | 31.6 | 4.8 | 3.01 | 1.64 |
| FeO | 23.5 | 18.6 | 12.8 | 13.6 | <b.dl | <b.dl | <b.dl | <b.dl | 8.4 | 11.3 | 10.1 |
| MgO | 37.7 | 42 | 46.8 | 44.9 | <b.dl | <b.dl | <b.dl | <b.dl | 15.7 | 17.2 | 15.7 |
| CaO | <b.dl | <b.dl | <b.dl | <b.dl | 15.3 | 12.7 | 16.9 | 15.7 | 21 | 15.76 | 27.3 |
| $Na_2O$ | <b.dl | <b.dl | <b.dl | <b.dl | 2.5 | 4.53 | 1.73 | 2.72 | <b.dl | <b.dl | <b.dl |
| Total | 100 | 99.9 | 100 | 99.9 | 100 | 100 | 100.03 | 100.02 | 100.1 | 99.6 | 100 |
| | End-Members | | | | | | | | | | |
| Fo | 74 | 80 | 86 | 85 | | | | | | | |
| Fa | 26 | 20 | 14 | 15 | | | | | | | |
| Ab | | | | | 78 | 60 | 85 | 76 | | | |
| An | | | | | 22 | 40 | 15 | 24 | | | |
| En | | | | | | | | | 44 | 49 | 38 |
| Wo | | | | | | | | | 42 | 33 | 48 |
| Fs | | | | | | | | | 13 | 18 | 14 |
| b.dl: below detection limit | | | | | | | | | | | |
| c: core, r: rim | | | | | | | | | | | |

| Table 2. Whole-rock major and trace element compositions of the Santorini basalt lavas. | | | | | | | | | |
|---|---|---|---|---|---|---|---|---|---|
| **Samples** | **7A** | **7B** | **8A** | **8B** | **9A** | **9b** | **PACS-2 given content**** | **PACS-2 measured content**** | **Relative uncertainty %** |
| **$SiO_2$** | 51.1 | 50.6 | 50.8 | 51 | 50.5 | 50.7 | 59 | 58.01 | 1.68 |
| **$TiO_2$** | 0.85 | 0.83 | 0.84 | 0.84 | 0.82 | 0.83 | 0.74 | 0.73 | 1.49 |
| **$Al_2O_3$** | 18.1 | 18.5 | 18.1 | 18.1 | 18.2 | 18 | 12.5 | 12.03 | 3.78 |
| **$Fe_2O_3$** | 8.96 | 8.73 | 8.97 | 8.94 | 8.15 | 8.84 | 5.85 | 5.96 | 1.88 |
| **MnO** | 0.15 | 0.15 | 0.15 | 0.15 | 0.15 | 0.15 | 0.057 | 0.059 | 3.51 |
| **MgO** | 5.39 | 6.24 | 6.25 | 6.13 | 6.35 | 5.97 | 2.44 | 2.39 | 1.97 |
| **CaO** | 10.7 | 10.6 | 10.7 | 10.7 | 10.8 | 10.7 | 2.75 | 2.81 | 2.22 |
| **$Na_2O$** | 2.24 | 2.14 | 2.12 | 2.14 | 2.04 | 2.03 | 5 | 4.89 | 2.14 |
| **$K_2O$** | 0.53 | 0.41 | 0.44 | 0.45 | 0.41 | 0.46 | 1.49 | 1.52 | 1.74 |
| **$P_2O_5$** | 0.09 | 0.11 | 0.1 | 0.12 | 0.09 | 0.13 | 0.22 | 0.23 | 3.4 |
| **LOI** | 1.12 | 1.6 | 1.05 | 0.95 | 2.1 | 2.07 | | | |
| **Total** | 99.23 | 99.91 | 99.52 | 99.52 | 99.61 | 99.88 | 90.047 | 88.629 | |
| Rb | 9.6 | 8.7 | 7.7 | 8.3 | 8.1 | 8.7 | | | |
| Ba | 107 | 88 | 81 | 84 | 86 | 107 | | 802 | - |
| Th | 11 | 9 | 10 | 11 | 11 | 9 | 0.6 | | |
| Nb | 2.6 | 2 | 2.2 | 2.6 | 2.1 | 3.1 | | | |
| La | 16.7 | 3.1 | 3.5 | 5.7 | 7.3 | 19 | | | |
| Ce | 27 | 22 | 11 | 19 | 59 | 69 | | | |
| Sr | 212 | 204 | 205 | 208 | 206 | 212 | 276 | 300 | 8.96 |
| Nd | 12 | 13 | 6 | 2 | 34 | 39 | | | |
| Zr | 63 | 57 | 56 | 56 | 55 | 58 | | | |
| Hf | 11 | 5 | 8 | 10 | 12 | 6 | | | |
| Y | 18.3 | 18.5 | 18.7 | 18.6 | 18.7 | 18.5 | | | |
| Ni | 38 | 51 | 51 | 51 | 34 | 30 | 40 | 39 | 2.48 |
| Zn | 51 | 52 | 46 | 50 | 51 | 52 | 364 | 344 | 5.39 |
| Sb | 2.9 | 3.5 | 2.9 | 3.2 | 2.9 | 3.2 | | | |
| Co | 14 | 30 | 25 | 27 | 14 | 14 | 11.5 | 11.5 | 0 |
| Cr | 82 | 98 | 93 | 103 | 112 | 88 | 91 | 94 | 4.07 |
| Cu | 36 | 56 | 59 | 55 | 30 | 20 | 310 | 326 | 5.14 |
| Ga | 14 | 12 | 13 | 13 | 13 | 13 | | | |
| Mo | 1.4 | 1.3 | 1.1 | 1.2 | 1.1 | 1.1 | 5.43 | 5.6 | 3.13 |

| | | | | | | | | | |
|---|---|---|---|---|---|---|---|---|---|
| Sc | 34 | 27 | 27 | 31 | 37 | 36 | | | |
| V | 153 | 199 | 196 | 186 | 199 | 192 | 133 | 143 | 7.29 |

The detection limits are: (1) 0.01 wt.% for $SiO_2$, $TiO_2$, $Al_2O_3$, $Fe_2O_3$, MgO, MnO, CaO, $Na_2O$, $K_2O$, and $P_2O_5$; (2) 0.002 wt.% for $SO_3$; (3) 0.005 wt.% for Ba and Pb; (4) 0.002 wt.% for Cu; (5) 0.001 wt.% for V, Co, Cr, Ni, Sr, Zn, and Zr; (6) 0.0001 wt.% for Mo, Nb, Rb, Sb, and Sc; and (7) <0.0009 wt.% for Ce, Ga, Th, and Y.

**: Given and measured content based on 10 replicate analyses.

**Table 3. Calculated results of primary basalt magma by PRIMACALC2 and its source conditions estimated by ABS5 models.**

| Model | PRIMACALC2 | | | ABS5 | | |
|---|---|---|---|---|---|---|
| Element | Input | Chamber | Mantle | Element | Mantle | |
| Sample | Santorini | Santorini | P. basalt | Sample | P. Basalt | 1SD |
| $SiO_2$ | **50.71** | 52.41 | 46.67 | $SiO_2$ | 48.66 | 0.63 |
| $TiO_2$ | **0.84** | 0.87 | 0.49 | $TiO_2$ | 0.78 | 0.09 |
| $Al_2O_3$ | **18.26** | 18.88 | 16.40 | $Al_2O_3$ | 14.04 | 0.29 |
| FeO | **7.31** | 7.55 | 9.45 | FeO | 9.81 | 0.66 |
| MnO | **0.15** | 0.16 | 0.12 | MnO | - | - |
| MgO | **6.07** | 6.28 | 13.86 | MgO | 15.44 | 0.41 |
| CaO | **10.77** | 11.13 | 11.43 | CaO | 9.68 | 0.42 |
| $Na_2O$ | **2.11** | 2.18 | 1.34 | $Na_2O$ | 1.35 | 0.00 |
| $K_2O$ | **0.44** | 0.45 | 0.20 | $K_2O$ | 0.21 | 0.00 |
| $P_2O_5$ | **0.09** | 0.10 | 0.04 | $P_2O_5$ | 1.55 | 0.60 |
| SUM | **99.68** | 100.00 | 100.00 | SUM | | |
| Rb | **8.02** | - | 3.96 | Rb | 4.50 | 0.10 |
| Ba | **86.9** | - | 45.1 | Ba | 80.1 | 6.34 |
| Th | *1.0* | - | 0.59 | Th | 0.32 | 0.02 |
| U | *0.20* | - | 0.15 | U | 0.21 | 0.02 |
| Nb | **2.35** | - | 1.15 | Nb | 1.23 | 0.03 |
| Ta | *0.15* | - | 0.07 | Ta | 0.06 | 0.00 |
| K | **3616** | - | 1837 | K | 1733 | 29.93 |
| La | **8.26** | - | 3.78 | La | 3.48 | 0.05 |
| Ce | **26.3** | - | 7.6 | Ce | 11.8 | 0.09 |
| Pb | *3.00* | - | 1.32 | Pb | 1.48 | 0.09 |
| Pr | *3.00* | - | 1.13 | Pr | 1.18 | 0.03 |
| Sr | **208** | - | 226 | Sr | 244 | 21.69 |
| Nd | **12.8** | - | 5.20 | Nd | 5.00 | 0.17 |
| Sm | *3.00* | - | 1.64 | Sm | 1.14 | 0.05 |
| Zr | **55.3** | - | 36.5 | Zr | 32.8 | 0.73 |
| Hf | **1.30** | - | 1.10 | Hf | 1.05 | 0.02 |
| Eu | 0.90 | - | 0.56 | Eu | 0.43 | 0.01 |

| | | | | | | |
|---|---|---|---|---|---|---|
| Gd | *3.00* | - | 1.88 | Gd | 1.54 | 0.03 |
| Tb | 0.50 | - | 0.32 | Tb | 0.28 | 0.01 |
| Dy | *3.30* | - | 2.09 | Dy | 1.95 | 0.04 |
| Y | **18.6** | - | 10.1 | Y | 11.6 | 0.19 |
| Ho | *0.70* | - | 0.44 | Ho | 0.42 | 0.01 |
| Er | *2.00* | - | 1.25 | Er | 1.25 | 0.02 |
| Tm | *0.30* | - | 0.19 | Tm | 0.20 | 0.00 |
| Yb | 2.00 | - | 1.22 | Yb | 1.31 | 0.03 |
| Lu | 0.30 | - | 0.18 | Lu | 0.19 | 0.00 |
| $H_2O$ (wt%) in basalt | - | - | 1.01 | $H_2O$ (wt%) in basalt | 1.55 | 0.60 |
| Ni (wt%) in olivine | - | - | 0.34 | Pslab (GPa) | 4.4 | 0.1 |
| Fo% in olivine | - | - | 91.00 | Tslab (°C) | 799 | 1 |
| Mg# in basalt | - | - | 0.76 | Fliq(AOC) | 0.90 | 0.02 |
| $Fe^{2+}/Fe^{(t)}$ in basalt | - | - | 0.78 | Fliq(SED) | 0.07 | 0.02 |
| T (°C) in chamber/mantle | - | 1124 | 1358 | %R slab | 138 | 4 |
| P (GPa) in chamber/mantle | - | 0.02 | 2.10 | %MORBext. | 5.5 | 2.8 |
| % crystallization | - | 70 | - | fslb liq. (%) | 5.4 | 1.6 |
| MgO (wt%) in mantle | - | - | 43 | $H_2O$ in slab liq. (%) | 4.9 | 1.7 |
| T (°C) in mantle | - | - | 1353 | T (°C) in mantle | 1323 | 21 |
| P (GPa) in mantle | - | - | 2.1 | P (GPa) in mantle | 1.7 | 0.1 |
| F (%) | - | - | 7.6 | F (%) | 18.5 | 5.1 |
| Input column indicates avaerage composition of the Santorini basalt. | | | | | | |
| Data are from this study (bold), from Michaud et al. (2000) (regular), or estimated from other elements (italic). | | | | | | |
| P. Basalt: Primary basalt; 1SD: 1-standard deviation | | | | | | |

**Supporting Information Table S1.** Results of PRIMACALC2 calculations for forward modeling of crystallization sequence from primary basalt to target Santorini basalt.

**Supporting Information Table S2.** Target basalt, calculated basalt, slab liquid, and source compositions used in ABS5 calculations.

Highlights

- -Geochemical modeling shows slab flux to Santorini source derives from ~145 km depth (84)
- -Primitive Santorini basalt formed by 18% fluxed partial melting at 1323°C and 1.7 GPa (85)
- -Dehydration of steep slab and deep partial melting yield narrow Hellenic volcanic arc (85)

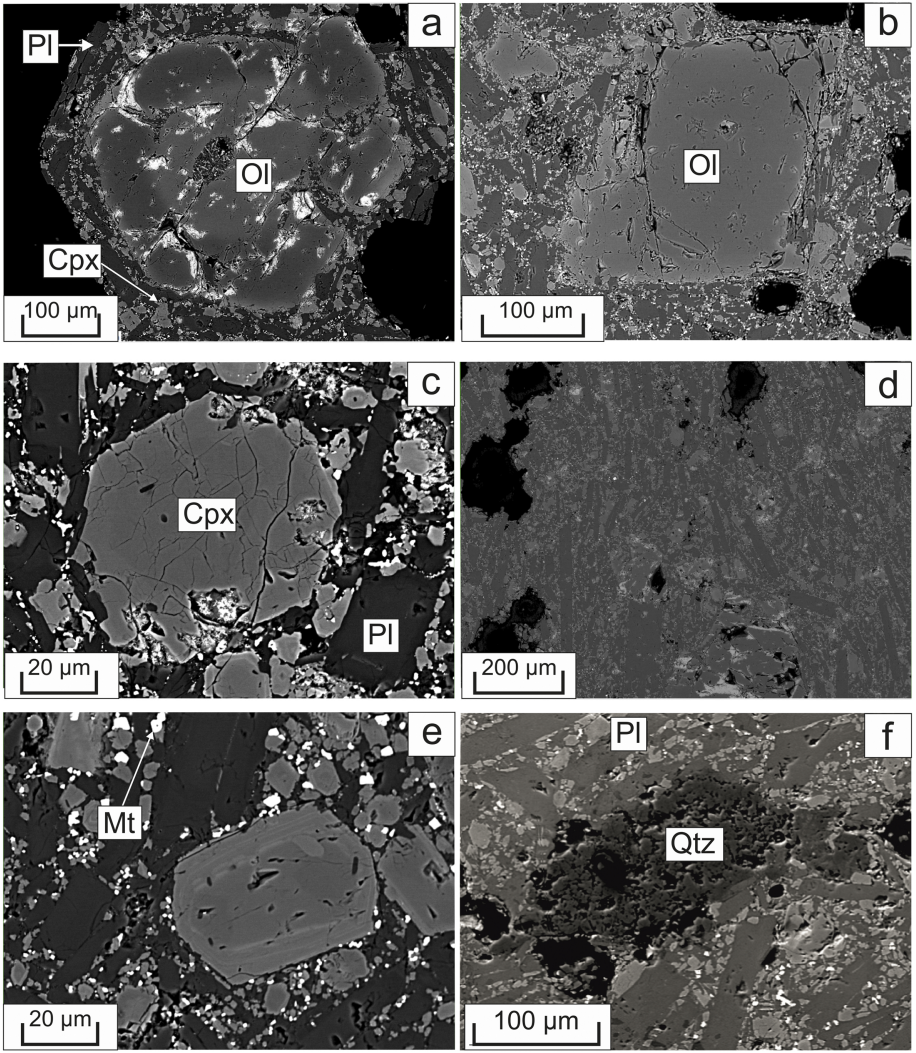
a
Pl
Ol
Cpx
100 µm
b
Ol
100 µm
c
Cpx
Pl
20 µm
d
200 µm
e
Mt
20 µm
f
Pl
Qtz
100 µm

Figure 1

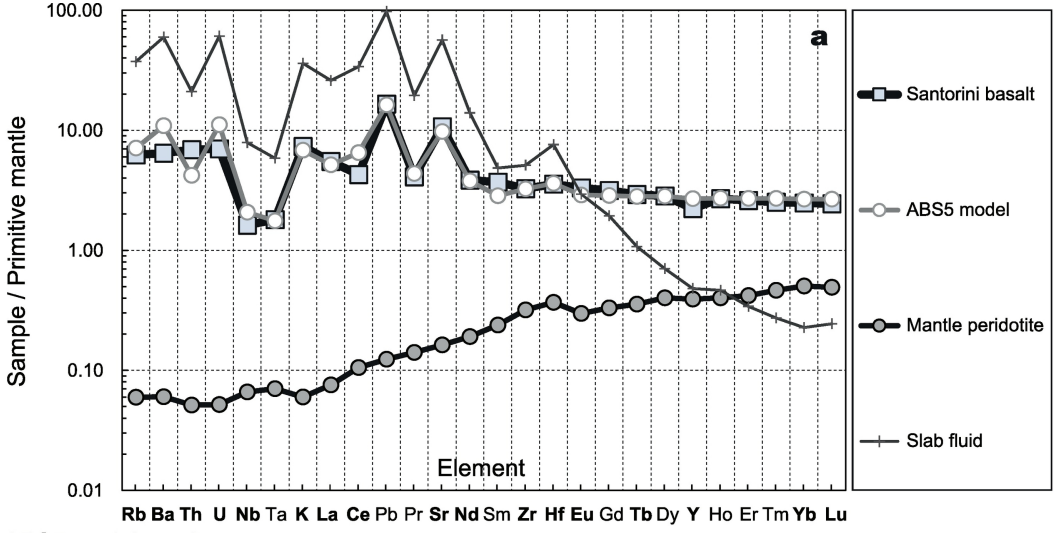


ABS5 model results

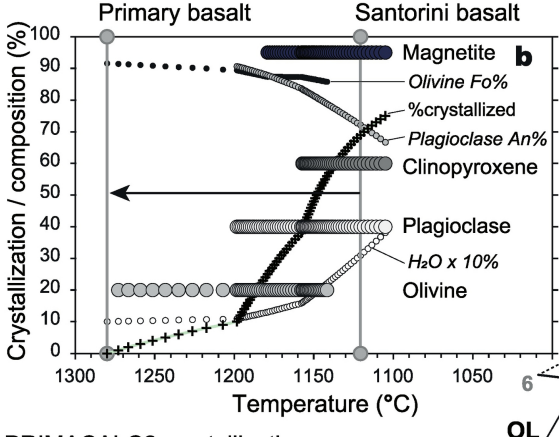


PRIMACALC2 crystallization sequence

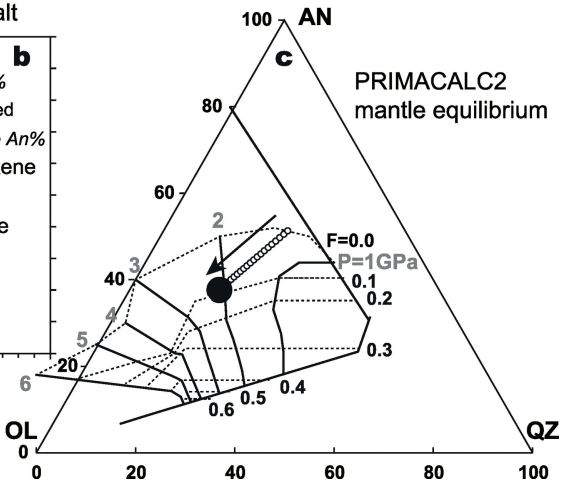


Figure 2

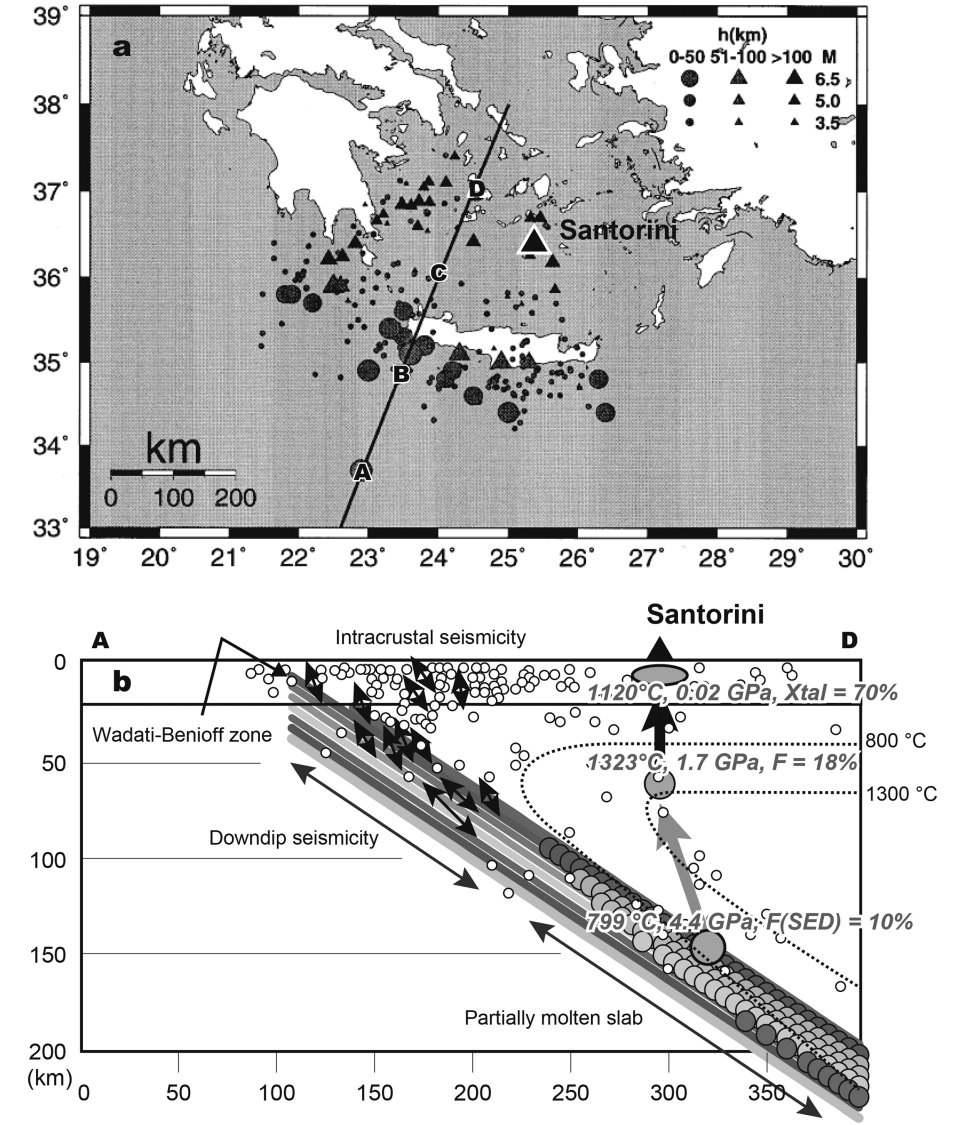
a
h(km)
0-50 51-100 >100 M
6.5
5.0
3.5
Santorini
A
B
C
D
km
0 100 200
39°
38°
37°
36°
35°
34°
33°
19° 20° 21° 22° 23° 24° 25° 26° 27° 28° 29° 30°
b
Santorini
A
D
Intracrustal seismicity
Wadati-Benioff zone
Downdip seismicity
Partially molten slab
1120°C, 0:02 GPa, Xtal = 70%
1323°C, 1.7 GPa, F = 18%
799°C, 4.4 GPa, F(SED) = 10%
800 °C
1300 °C
0
50
100
150
200
(km)
0 50 100 150 200 250 300 350

Figure 3